Stabilization of small polarons in $BaTiO_3$ by local distortions

Naoki Tsunoda,[1] Yu Kumagai,[1,2,3,*] and Fumiyasu Oba[1,2,4]

[1]*Laboratory for Materials and Structures, Institute of Innovative Research, Tokyo Institute of Technology, Yokohama 226-8503, Japan*

[2]*Materials Research Center for Element Strategy, Tokyo Institute of Technology, Yokohama 226-8503, Japan*

[3]*PRESTO, Japan Science and Technology Agency, Tokyo 113-8656, Japan*

[4]*Center for Materials Research by Information Integration, Research and Services Division of Materials Data and Integrated System, National Institute for Materials Science, Tsukuba 305-0047, Japan*

(Received 25 April 2019; revised manuscript received 8 July 2019; published 27 November 2019)

Small polarons and point defects in $BaTiO_3$ are investigated using hybrid functional calculations. Based on the experimentally-confirmed order-disorder-type phase transitions, Ti displacements along ⟨111⟩ directions are included in the cubic model. We reveal that the self-trapped electrons at Ti sites are stable in both rhombohedral and cubic $BaTiO_3$ and the Ti off-centering, which introduces antibonding hybridization between lowest-lying Ti-3*d* and O-2*p* orbitals at the conduction band minimum, is essential for stabilizing the self-trapped electrons. Our calculations are in contrast to previous theoretical studies, even qualitatively, but reasonably consistent with the long-standing experimentally-observed small polarons in $BaTiO_3$. This finding may explain why self-trapped electrons are not stable in $SrTiO_3$ but are in $BaTiO_3$ from the symmetry viewpoint.

DOI: 10.1103/PhysRevMaterials.3.114602

Introduction. $BaTiO_3$ (BTO), a prototypical perovskite oxide, is a key material for both scientific research and industrial applications thanks to its fascinating physical properties, such as high dielectric constant [1], ferroelectricity [2], nonlinear optical properties [3], and anomalous electrical resistivity at the Curie temperature [4]. Because of its importance in electronics, such as in ceramic capacitors [5] and thermistors [6], most of the physical properties have been experimentally established in the last 60 years. However, the understanding of several phenomena (e.g., carrier transportation, positive temperature coefficient resistivity effect, and phase transitions) at the atomic and electronic scales is still limited although many experimental/theoretical studies have been reported.

Small polarons generally play important roles in electronic and ionic transport, optical properties, and charge compensations. In BTO, it has been experimentally reported that small polarons would be the origin of the green luminescence [7–9], mid-near-infrared absorption, and blue coloration [10–14]. Especially, the transport of charged carriers has been attributed to hopping of small polarons in some studies [15–19]. In addition, Ti^{3+} centers are often observed by electron paramagnetic resonance (EPR) measurements in *n*-doped BTO [20–22]. Based on these experimental observations, donor electrons in BTO are considered to take the form of small polarons at the Ti sites and couple with donor-type defects that form deep states especially at low temperature. Furthermore, the hopping of small polarons indicates that the isolated small polarons, or self-trapped electrons (STEs), are also stable in BTO.

However, the theoretical studies based on first-principles calculations that have been conducted to date seem to be inconsistent with the polaronic behavior. For instance, Choi *et al.* [23] revealed that the oxygen vacancies (V_O) exhibit a hydrogenic shallow donor state as a ground state using the Heyd-Scuseria-Ernzerhof (HSE06) hybrid functional [24,25]. Baker *et al.* also calculated various types of point defects in BTO and $SrTiO_3$ using HSE and showed that V_O and Nb-on-Ti impurities act as shallow donors in both cases [26]. Liu *et al.*, using generalized gradient approximation (GGA) with Hubbard $+U$ correction (GGA $+ U$) and HSE with 30% of the Fock exchange, found that STEs are energetically unfavorable [27,28]. These discrepancies from the experimental findings motivated us to revisit the small polarons and point defects in BTO.

Modeling of Ti off-centered atomic structures. In the previous theoretical studies, the $Pm\bar{3}m$ highly-symmetric structure model, whose unit cell is composed of five atoms, was adopted. However, we consider that this model is not adequate for point defect calculations in BTO because of the following two reasons. First, a series of rhombohedral-orthorhombic-tetragonal-cubic phase transitions in BTO is considered to be an order-disorder type, based on the recent analysis of local atomic structures [29,30]. Therefore, the Ti off-centering should persist in the microscopically highly-symmetric *Amm*2, *P*4*mm*, and $Pm\bar{3}m$ phases. Indeed, the Ti displacements play a significant role to stabilize the STEs, as will be discussed later. Second, the high symmetry model includes strong imaginary phonon modes (See Fig. S6 in the Supplemental Material [31] for calculated phonon bands). In that case, if the symmetry is lowered by introducing a defect, these unstable phonon modes will spontaneously develop in the entire supercell containing the defect. As a result, the

*yuuukuma@gmail.com

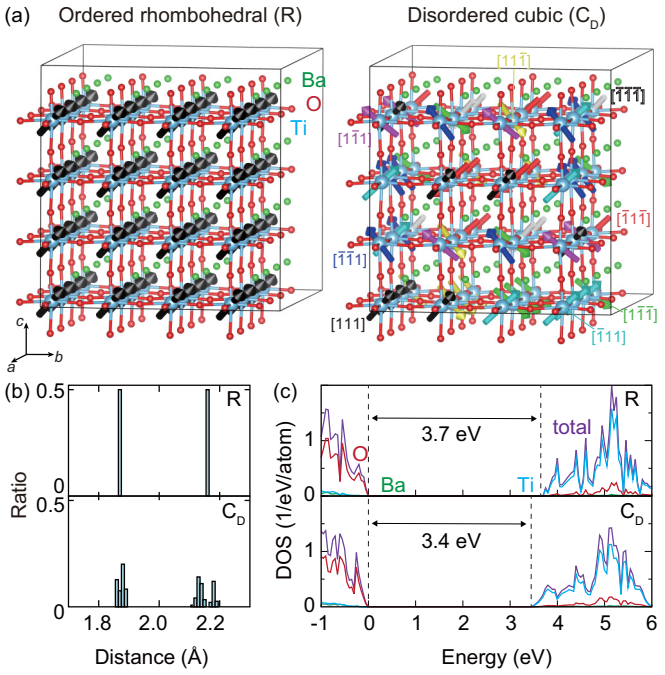

FIG. 1. (a) Rhombohedral model (R) and cubic model with disordered Ti displacements (C_D) composed of 320 atoms that are used for the point defect calculations in BTO. Ti displacements along the ⟨111⟩ directions are visualized by the arrows at the center of the TiO_6 octahedra with different colors depending on the displacement direction (see text for details of C_D). (b) Ti-O bond length distributions in the R and C_D models. (c) Total and site-projected DOS for the R and C_D models calculated using HSE06. Zero of the energy is set to each valence-band maximum.

defect formation energy, estimated from the energy difference from that of the highly-symmetric pristine supercell, decreases with increasing the supercell size and diverges to minus infinity. (See Supplemental Material for the cell size dependence of the oxygen vacancy formation energy in the highly-symmetric cubic model.) Thus, in principle, calculations of the defect formation energies using a supercell with any unstable phonon modes should be inadequate (e.g., cubic $SrTiO_3$ shows an unstable octahedral rotation mode).

We therefore need to calculate the point defects and small polarons with a more realistic order-disorder-type cubic BTO model with displaced Ti atoms in the ⟨111⟩ directions. We constructed such a model using Monte Carlo simulated annealing based on the eight-bit model Hamiltonian proposed in Ref. [30]. In this Hamiltonian, Ti ions are shifted in one of the eight ⟨111⟩ directions while keeping some correlations favorable from the view of electrostatics. Here, we adopted a $4 \times 4 \times 4$ 320-atom supercell. Figure 1(a) shows our cubic model with displaced Ti ions (C_D) as well as the rhombohedral one composed of the same number of atoms (R) (see the Supplemental Material for other disordered models). For C_D, we adopted a snapshot structure where the averaged polarization becomes zero along any direction, which is a prerequisite for satisfying the macroscopically averaged cubic symmetry. Note that since the atomic positions are not symmetrically constrained, any unstable phonon modes are absent in C_D. We first fully relaxed both structures using the HSE06 hybrid functional. We note that when several-disordered C_D structures are relaxed using the modified Perdew-Burke-Ernzerhof GGA tuned for solids [32] (PBEsol), all the models tend to relax to the R phase, irrelevant to the degree of disorder and/or the supercell sizes up to 1080 atoms. The reason is not so obvious but probably because electrons tend to uniformize by the self-interaction errors in the GGA. Indeed, the polar distortion and relative stability of the R phase from the highly-symmetric cubic phase are much smaller in PBEsol (see also Table S1 in the Supplemental Material for functional dependencies of phase stability and structural details of high and low symmetry phases).

After structure relaxation, the volume and total energy of C_D are different only by -0.13% and $+3.1$ meV/atom from those of R, respectively. The Ti-O length distributions in both R and C_D [Fig. 1(b)] show double peak features, which indicates Ti off-centering persists in C_D yet its displacement distributions are broadened. The HSE06 calculated density of states (DOS) is also shown in Fig. 1(c). As expected from the similarity in the Ti displacement distribution, the electronic structures of R and C_D are very close to each other, but several peaks in the R phase are broadened in C_D. Consequently, tail states at the band edges develop, and the band gap is slightly lowered from 3.69 eV in R to 3.4–3.5 eV in C_D. Note that the experimental band gap for the cubic phase is 3.2 eV at 420 K with a rate of 4.5×10^{-4} eV/K [33] and is extrapolated to 3.4 eV at 0 K [34], which agrees well with that of our C_D model. In contrast, when using the highly-symmetric $Pm\bar{3}m$ model, the band gap is greatly reduced to 2.95 eV.

Small polarons and point defects. We next discuss the energetics and electronic structures of STEs, native defects, and hydrogen impurities in the R and C_D models. The formation energy of a point defect under a thermodynamically equilibrium condition is calculated as

$$E_f[D^q] = \{E[D^q] + E_{\mathrm{corr}}[D^q]\} - E_P + \sum n_i \mu_i + q(\epsilon_{\mathrm{VBM}} + \Delta\epsilon_F), \quad (1)$$

where $E[D^q]$ and E_P are the total energies of the supercell with defect D in charge state q and the supercell without a defect, respectively. n_i is the number of removed ($n_i > 0$) or added ($n_i < 0$) i-type atoms and μ_i is the chemical potential representing the growth conditions. In this study, the chemical potentials are set such that BTO is stable in the chemical potential diagram (see the Supplemental Material). ϵ_{VBM} is the energy level of the valence band maximum (VBM) in each pristine cell, and $\Delta\epsilon_F$ represents the Fermi level with respect to ϵ_{VBM}. $E_{\mathrm{corr}}[D^q]$ corresponds to an energy for correcting a finite supercell size error [35–37]. In this study, we were especially careful to correct the oxygen vacancy formation energies with long-ranged atomic relaxation along the -Ti-V_O-Ti- chain direction [37]. See method and the Supplemental Material for details of the finite supercell size corrections. Recently, deviations from linearity of total energy as a function of the electron number, so-called nongeneralized Koopman's energy (Δ_{XC}) have been calculated for evaluating the accuracy of the functional adopted. We have also calculated Δ_{XC} based on the method of Ref. [38] (see Table S2 in the Supplemental Material for Δ_{XC} as a function of the Fock-exchange fraction.) and have found that Δ_{XC} for STE is -0.15 eV for both R and

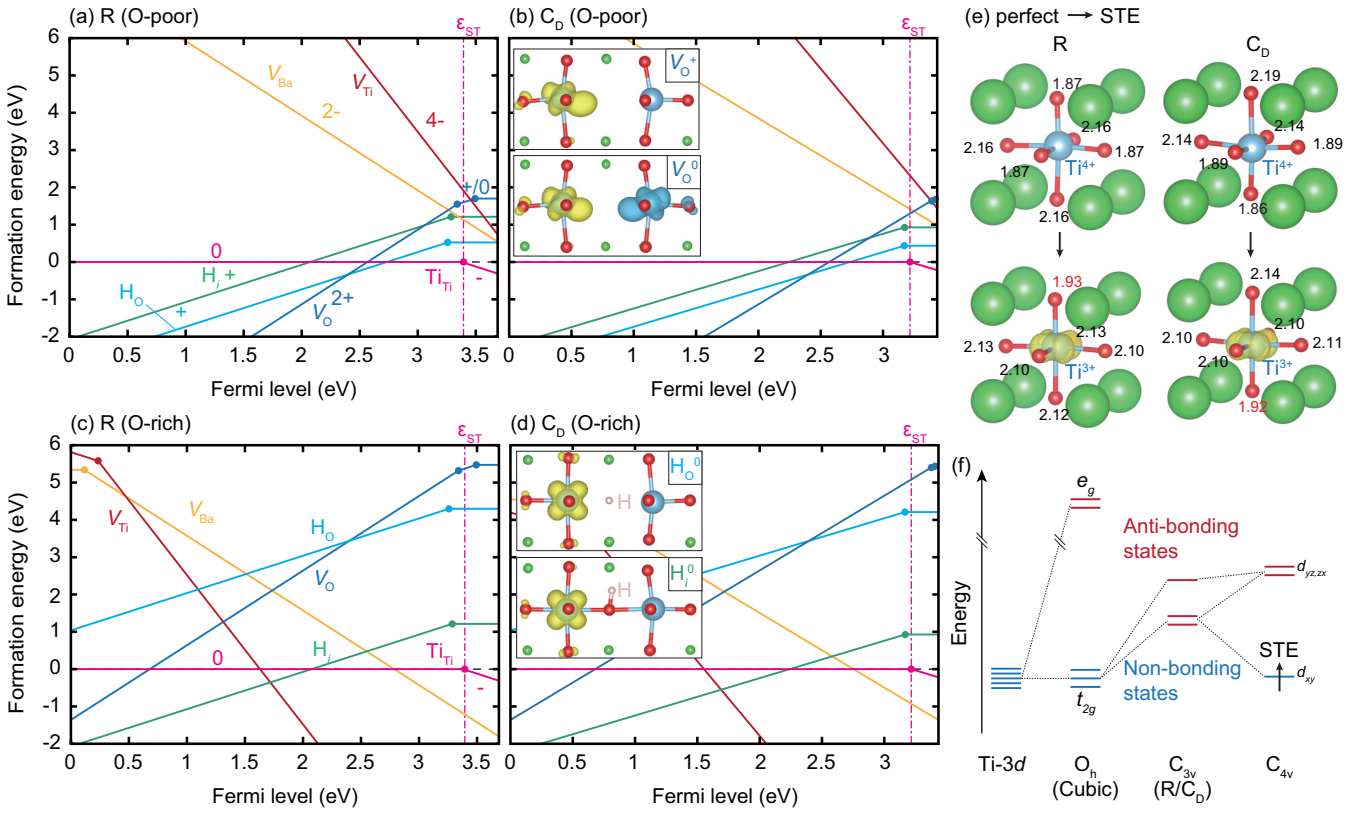

FIG. 2. Formation energies of the self-trapped electrons (STEs) and point defects as a function of the Fermi level at [(a),(b)] O-poor and [(c),(d)] O-rich conditions in the [(a),(c)] R and [(b),(d)] C_D models. Zero of the Fermi level and its upper limit is set to each valence-band maximum and conduction-band minimum, respectively. The defect species and sites are indicated by X_Y, where X is a vacancy (V) or an added element and Y is an interstitial site (i) or a substitutional site. The chemical potentials are set at a condition where BaO and O_2 equilibrate with BTO at the O-rich condition, whereas TiO_2 and Ti_2O_3 at the O-poor condition (e.g., $T = 1473$ K, $P_{O_2} = 10^{-10}$ Pa). We assume the latter condition is the lower case of the O chemical potential reported in [34] (see the Supplemental Material for details). The insets of [(b),(d)] show local atomic structures and squared wave functions corresponding to the small polaron levels in V_O^+, V_O^0, H_i^0, and H_O^0 in the C_D model. Different spin states in V_O^0 are distinguished by yellow and blue colors. The isosurfaces are set at 10% of each maximum value. (e) Local atomic structures before and after structure relaxation near the Ti ion with an STE. The Ti-O distances are shown in Å. (f) Schematic illustration for the energy levels of the Ti-3d orbitals surrounded by six oxygen ions. Here, we consider a Ti^{4+} ion in the O_h and C_{3v} site symmetries and a Ti^{3+} ion trapping a small polaron in the C_{4v} symmetry (see text for details). Note that hybridization of t_{2g} (d_{xy}) orbitals with O-2p orbitals is absent at the Γ point in the O_h (C_{4v}) symmetry.

C_D models. Therefore, we discuss defect formation energies and defect-involving luminescences within this accuracy.

With defect notation, STE can be written as Ti_{Ti}^{-} since a small polaron is trapped at the Ti site. The STE stabilization energy then corresponds to $E_f[Ti_{Ti}^{-}]$ at the Fermi level locating at the conduction band minimum (CBM). Since all the atomic sites are symmetrically inequivalent in C_D, we checked the site differences in the formation energies by calculating V_O^{2+} and Ti_{Ti}^{-} at three randomly chosen sites for each and found that they are within only 0.05 eV in both cases. Thus, the lowest energy results are shown hereafter and sites for other defects in C_D were randomly chosen based on this validation.

Figures 2(a)–2(d) show the defect formation energies as a function of the Fermi level. The most noteworthy result in Fig. 2 is that the STEs are stable in both the R and C_D models with self-trapping energies of 0.3 and 0.2 eV, respectively [39]. We have found that the TiO_6 local structures near the Ti ions capturing a small polaron are modified from the ⟨111⟩ off-centering distortions to tetragonal-like distortions, as shown in Fig. 2(e). This is because in the rhombohedral phase, the Ti site holds the C_{3v} site symmetry, where the doubly degenerated Ti-3d orbitals at the CBM construct antibonding states with the neighboring O-2p orbitals (see the Supplemental Material for band structures of BTO). However, when one electron is occupied, the local geometry is modified to reduce the antibonding hybridization at the lowest occupied energy orbital [Fig. 2(f)]. Therefore, such hybridization between the lowest energy Ti-3d orbitals and O-2p orbitals, accompanied by the TiO_6 local distortion, stabilizes the STE. In light of the above discussion, STEs would be stable even in orthorhombic and tetragonal BTO as Ti displacements along the ⟨111⟩ directions persist in these phases, based on experiments [40]. Conversely, an excess electron is not self trapped but delocalizes as a conduction band state in the highly symmetric cubic phase. This also indicates the Ti off-centering plays a crucial role for electron self trapping.

It is easily expected that these small polarons are trapped by donor-type defects. Indeed, V_O, interstitial hydrogen (H_i), and substitutional hydrogen on the oxygen site (H_O) capture localized polaronic electrons [see insets in Figs. 2(b) and

2(d)]. These small polarons show nonbonding characteristics as STEs. However, contrary to the electrostatics viewpoint, the couplings of small polarons and defects are not always exothermic; V_O show shallower transition levels than STE especially in C_D, which means the coupling of V_O^{2+} and small polarons is energetically unfavorable. This would be because V_O^{2+} in Ti perovskite oxides commonly construct long-ranged atomic relaxation along the -Ti-V_O-Ti- chain structure accompanied by dynamic charge transfers [37]. Such widespread defect charge distribution relatively decreases the V_O formation energy as its charge state is increased. Furthermore, when two polarons are captured near V_O, their repulsive interactions should also increase the formation energy [41].

H_i and H_O show relatively small atomic modifications and deeper transition levels than STE. Thus, H_O and H_i prefer to be coupled with small polarons in the *n*-type regime. In such cases, hydrogen diffusivity should be drastically decreased. It is noteworthy that the most stable hydrogen state changes from a positively-charged proton (H_i) to a negatively-charged hydride substituted on the oxygen site (H_O) when the oxygen chemical potential (μ_O) is lowered less than 3.1 eV (e.g., $T =$ 1223 K, $P_{O_2} = 10^{-10}$ Pa) in both the R and C_D models.

Among the acceptors, Ti vacancies in the 4- charge state (V_{Ti}^{4-}) become dominant at the O-rich condition [Figs. 2(c) and 2(d)]. The Fermi levels are thereby pinned at a position lower than the transition levels of the small polarons. Indeed, in the EPR measurement, the intensity of Ti^{3+}-related signals decreases after oxidizing in an O_2 atmosphere [21]. In terms of *p*-type dopability, even at this condition, the energy of V_O^{2+} is not increased so high and consequently imposes the lower limit of the Fermi level. Furthermore, we have found the self-trapped hole (STH) is also stable by 0.25 eV and 0.29 eV in the R and C_D phases, respectively, which are close to the previously reported self-trapping energy of 0.2 eV in highly symmetric cubic BTO [42]. Thus, it seems difficult to achieve the *p*-type BTO even if shallow acceptor dopants exist and V_O is well suppressed by a growth technique.

Here we compare our calculations with experimentally observed green luminescences in BTO [7–9]. We estimated optical transition energies of defects involving electron small polarons at a fixed ground state atomic position based on the Franck-Condon principle [43]. Image charge corrections are applied following Ref. [44]. Calculated recombination energies of the electron polarons (Ti_{Ti}^{-}, V_O^{+}, V_O^{0}, H_O^{0}, and H_i^{0}) with a hole at the VBM are 2.1–2.3 eV and 2.0–2.3 eV for the R and C_D models, respectively, which are close to the experimental values of 2.4–2.5 eV [7–9]. Recently, Traiwattanapong *et al.* have reported recombination energy of a STH and an electron at the CBM to be 2.17 eV [42], which is close to our calculated 2.33 and 2.04 eV in the R and C_D phases, respectively. Therefore, the electron polarons, hole polarons, or both may be the origin of the green luminescences in BTO.

Compared with the optical properties, the carrier transport in BTO should be discussed more carefully because it is largely affected by the ferroelectric domain structure, grain boundary, and surface states. For example, the positive temperature coefficient resistivity effect is commonly observed in polycrystals but not in single crystals. In general, the small polaron's hopping model fits well the observed thermally activated conductivity especially in the rhombohedral phase [14,45–47]. The deep pinning level at 0.3 eV in the R model is consistent with this hopping scenario at low temperature [Fig. 2(a)]. When the Fermi level is located at the ϵ_{ST}, the calculated carrier-electron concentration is increased from 4.1×10^{12} cm^{-3} to 2.0×10^{18} cm^{-3} as the temperature increases from 200 K to 400 K [Figs. 2(a) and 2(b)]. This implies sufficient numbers of small polarons and delocalized carrier electrons coexist [48]. Indeed, at higher temperature, whether the carrier transport mechanism is small polaron hopping or band conduction is controversial or less discussed than at low temperature, even with single crystals. This would arise from the relatively small temperature dependencies and/or large anisotropy caused by domain structures [13–15,46,49–51].

We should mention that since potential energy as a function of the Ti displacement is softened with increasing temperature on account of the phonon anharmonicity, the Ti displacement should be reduced in reality compared with in our C_D model. Then, antibonding at the CBM is decreased, which leads to a lower CBM and shallower ϵ_{ST}. Therefore, it would be difficult to confidently conclude the polaronic scenario in high temperature phases, but we hope this work motivates researchers to conduct further investigations.

Conclusion. We have investigated the small polarons and point defects in $BaTiO_3$ from first principles using both the rhombohedral and disordered cubic models. For the cubic model, we considered the Ti displacements along the ⟨111⟩ directions based on the experimentally confirmed order-disorder type phase transitions. The Ti off-centering leads to antibonding between the Ti-3*d* and O-2*p* orbitals at the conduction band minimum. Therefore, the STE at the Ti site has room to reduce its energy by reducing the antibonding component by changing the local structure to be tetragonal-like. Consequently, the STEs are found to be energetically favorable in both phases compared with delocalized carrier electrons. Our results are in contrast to previous theoretical studies that used the centrosymmetric cubic model but reasonably explain some experimental observations such as green luminescence [7–9] and small polaron hopping conductivity at low temperatures [14,45–47]. This discussion is extendable to other d^0 perovskite oxides. For example, the absence of the Ti off-centering in cubic $SrTiO_3$ would partially explain why STEs are unstable in $SrTiO_3$ [52].

Methods. First-principles calculations were performed using the projector augmented wave (PAW) method [53,54], as implemented in VASP [55]. Ba 5*s* and 5*p*, Ti 3*d* and 4*s*, and O 2*s* and 2*p* were treated as valence electrons. The HSE06 hybrid functional [24,25] was used for all calculations. For the 320-atom supercell, the Γ point was used for the reciprocal space integration [56]. The residual forces were reduced to less than 0.01 and 0.04 eV/Å for pristine cell relaxations and defect calculations, respectively; the lattice constants were relaxed for the former while fixed for the latter. Spin polarization was considered in all the point-defect calculations. For finite supercell-size errors associated with spurious electrostatic interactions, the extended Freysoldt-Neugebauer-Van de Walle (eFNV) corrections [35,36] were adopted for small polarons and point defects. Exceptions are V_O^{+} and V_O^{2+} as they show one-dimensionally spread defect states that spill out from the 320-atom supercell [37]. Therefore, their correction

energies were estimated from the cell size dependences calculated using PBEsol (see the Supplemental Material for details). Atomic positions and squared wave functions of the defect states in Figs. 1 and 2 were visualized using VESTA [59].

Acknowledgments. We greatly appreciate N. Ohashi for fruitful discussion. This work was supported by the MEXT Elements Strategy Initiative to Form Core Research Center "Tokodai Institute for Element Strategy (TIES)," PRESTO (JPMJPR16N4), and the Support Program for Starting Up Innovation Hub MI^2I from JST, Japan. The computing resources of ACCMS at Kyoto University and Research Institute for Information Technology at Kyushu University were used for part of this work.

[1] H. Kumazawa and K. Masuda, Fabrication of barium titanate thin films with a high dielectric constant by a sol–gel technique, Thin Solid Films **353**, 144 (1999).

[2] M. N. Kamalasanan, S. Chandra, P. C. Joshi, and A. Mansingh, Structural and optical properties of sol-gel-processed $BaTiO_3$ ferroelectric thin films, Appl. Phys. Lett. **59**, 3547 (1991).

[3] S. Ducharme and J. Feinberg, Speed of the photorefractive effect in a $BaTiO_3$ single crystal, J. Appl. Phys. **56**, 839 (1984).

[4] B. Huybrechts, K. Ishizaki, and M. Takata, The positive temperature coefficient of resistivity in barium titanate, J. Mater. Sci. **30**, 2463 (1995).

[5] H. Kishi, Y. Mizuno, and H. Chazono, Base-Metal Electrode-Multilayer Ceramic Capacitors: Past, Present and Future Perspectives, Jpn. J. Appl. Phys. **42**, 1 (2003).

[6] H. Niimi, K. Mihara, Y. Sakabe, and M. Kuwabara, Preparation of Multilayer Semiconducting $BaTiO_3$ Ceramics Co-Fired with Ni Inner Electrodes, Jpn. J. Appl. Phys. **46**, 6715 (2007).

[7] M. Aguilar, C. Gonzalo, and G. Godefroy, X-ray induced luminescence from $BaTiO_3$, Solid State Commun. **30**, 525 (1979).

[8] M. Aguilar, C. Gonzalo, and G. Godefroy, Intrinsic luminescence from $BaTiO_3$ crystals, Ferroelectrics **25**, 467 (1980).

[9] H. Ihrig, J. H. T. Hengst, and M. Klerk, Conductivity-dependent cathodoluminescence in $BaTiO_3$, $SrTiO_3$ and TiO_2, Z. Phys. B: Condens. Matter **40**, 301 (1981).

[10] C. N. Berglund and H. J. Braun, Optical absorption in single-domain ferroelectric barium titanate, Phys. Rev. **164**, 790 (1967).

[11] P. Gerthsen, R. Groth, K. Hardtl, D. Heese, and H. Reik, The small polaron problem and optical effects in barium titanate, Solid State Commun. **3**, 165 (1965).

[12] G. W. Ross, P. Hribek, R. W. Eason, M. H. Garrett, and D. Rytz, Impurity enhanced self-pumped phase conjugation in the near infrared in 'blue' $BaTiO_3$, Opt. Commun. **101**, 60 (1993).

[13] M. Schrader, D. Mienert, T.-S. Oh, H.-I. Yoo, and K. D. Becker, An optical, EPR and electrical conductivity study of blue barium titanate, $BaTiO_{3-\delta}$, Solid State Sci. **10**, 768 (2008).

[14] J. Hwang, T. Kolodiazhnyi, J. Yang, and M. Couillard, Doping and temperature-dependent optical properties of oxygen-reduced $BaTiO_{3-\delta}$, Phys. Rev. B **82**, 214109 (2010).

[15] J. P. Boyeaux and F. M. Michel-Calendini, Small polaron interpretation of $BaTiO_3$ transport properties from drift mobility measurements, J. Phys. C **12**, 545 (1979).

[16] E. Iguchi, N. Kubota, T. Nakamori, N. Yamamoto, and K. J. Lee, Polaronic conduction in n-type $BaTiO_3$ doped with La_2O_3 or Gd_2O_3, Phys. Rev. B **43**, 8646 (1991).

[17] H. Ihrig and D. Hennings, Electrical transport properties of *n*-type $BaTiO_3$, Phys. Rev. B **17**, 4593 (1978).

[18] S. R. Gilbert, L. A. Wills, B. W. Wessels, J. L. Schindler, J. A. Thomas, and C. R. Kannewurf, Electrical transport properties of epitaxial $BaTiO_3$ thin films, J. Appl. Phys. **80**, 969 (1996).

[19] X. Jing, W. Xu, C. Yang, J. Feng, A. Zhang, Y. Zeng, M. Qin, M. Zeng, Z. Fan, J. Gao, X. Gao, G. Zhou, X. Lu, and J.-M. Liu, Tuning electrical conductivity, charge transport, and ferroelectricity in epitaxial $BaTiO_3$ films by Nb-doping, Appl. Phys. Lett. **110**, 182903 (2017).

[20] S. Lenjer, O. F. Schirmer, H. Hesse, and T. W. Kool, Conduction states in oxide perovskites: Three manifestations of Ti^{3+} Jahn-Teller polarons in barium titanate, Phys. Rev. B **66**, 165106 (2002).

[21] T. Kolodiazhnyi and A. Petric, Analysis of point defects in polycrystalline $BaTiO_3$ by electron paramagnetic resonance, J. Phys. Chem. Solids **64**, 953 (2003).

[22] V. V. Laguta, A. M. Slipenyuk, I. P. Bykov, M. D. Glinchuk, M. Maglione, A. G. Bilous, O. I. V'yunov, J. Rosa, and L. Jastrabik, Electron spin resonance investigation of impurity and intrinsic defects in Nb-doped $BaTiO_3$ single crystal and ceramics, J. Appl. Phys. **97**, 073707 (2005).

[23] M. Choi, F. Oba, and I. Tanaka, Electronic and structural properties of the oxygen vacancy in $BaTiO_3$, Appl. Phys. Lett. **98**, 172901 (2011).

[24] J. Heyd, G. E. Scuseria, and M. Ernzerhof, Erratum: Hybrid functionals based on a screened coulomb potential, J. Chem. Phys. **124**, 219906 (2006).

[25] A. V. Krukau, O. A. Vydrov, A. F. Izmaylov, and G. E. Scuseria, Influence of the exchange screening parameter on the performance of screened hybrid functionals, J. Chem. Phys. **125**, 224106 (2006).

[26] J. N. Baker, P. C. Bowes, J. S. Harris, and D. L. Irving, Mechanisms governing metal vacancy formation in $BaTiO_3$ and $SrTiO_3$, J. Appl. Phys. **124**, 114101 (2018).

[27] X. Liu, T. S. Bjrheim, and R. Haugsrud, Formation and migration of hydride ions in $BaTiO_{3-x}H_x$ oxyhydride, J. Mater. Chem. A **5**, 1050 (2017).

[28] They found that small polarons coupled with V_O and H_O are unstable when using HSE but are stable when using GGA + U with a larger U value of 4.49 eV at the Ti-3d orbitals. However, Hubbard U corrections may erroneously decrease the orbital hybridizations. For example, in the GGA + U ($U = 4.49$ eV) calculations, cubic BTO without polar distortion is more stable than the rhombohedral BTO. See also Fig. S6 in the Supplemental Material.

[29] K. Tsuda and M. Tanaka, Direct observation of the symmetry breaking of the nanometer-scale local structure in the paraelectric cubic phase of $BaTiO_3$ using convergent-beam electron diffraction, Appl. Phys. Express **9**, 071501 (2016).

[30] M. S. Senn, D. A. Keen, T. C. A. Lucas, J. A. Hriljac, and A. L. Goodwin, Emergence of Long-Range Order in $BaTiO_3$ from Local Symmetry-Breaking Distortions, Phys. Rev. Lett. **116**, 207602 (2016).

[31] See Supplemental Material at http://link.aps.org/supplemental/10.1103/PhysRevMaterials.3.114602 for supporting figures and their detailed explanation to provide more details of the calculations.

[32] J. P. Perdew, A. Ruzsinszky, G. I. Csonka, O. A. Vydrov, G. E. Scuseria, L. A. Constantin, X. Zhou, and K. Burke, Restoring the Density-Gradient Expansion for Exchange in Solids and Surfaces, Phys. Rev. Lett. **100**, 136406 (2008).

[33] S. H. Wemple, Polarization Fluctuations and the Optical-Absorption Edge in $BaTiO_3$, Phys. Rev. B **2**, 2679 (1970).

[34] P. Erhart and K. Albe, Thermodynamics of mono- and di-vacancies in barium titanate, J. Appl. Phys. **102**, 084111 (2007).

[35] C. Freysoldt, J. Neugebauer, and C. G. Van de Walle, Fully *Ab Initio* Finite-Size Corrections for Charged-Defect Supercell Calculations, Phys. Rev. Lett. **102**, 016402 (2009).

[36] Y. Kumagai and F. Oba, Electrostatics-based finite-size corrections for first-principles point defect calculations, Phys. Rev. B **89**, 195205 (2014).

[37] N. Tsunoda, Y. Kumagai, M. Araki, and F. Oba, One-dimensionally extended oxygen vacancy states in perovskite oxides, Phys. Rev. B **99**, 060103 (2019).

[38] S. Lany, Predicting polaronic defect states by means of generalized koopmans density functional calculations, Phys. Status Solidi B **248**, 1052 (2011).

[39] When the Ti 3*s* and 3*p* electrons were also included as valence electrons, the self-trapping energy of STE in the R phase is slightly increased by only 0.02 eV.

[40] K. Tsuda, R. Sano, and M. Tanaka, Nanoscale local structures of rhombohedral symmetry in the orthorhombic and tetragonal phases of $BaTiO_3$ studied by convergent-beam electron diffraction, Phys. Rev. B **86**, 214106 (2012).

[41] V_O in the neutral charge state forms a bipolaron in a spin-singlet configuration composed of two Ti^{3+}, which are not detected by the EPR measurement.

[42] W. Traiwattanapong, A. Janotti, N. Umezawa, S. Limpijumnong, J. T-Thienprasert, and P. Reunchan, Self-trapped holes in $BaTiO_3$, J. Appl. Phys. **124**, 085703 (2018).

[43] C. G. Van de Walle and J. Neugebauer, First-principles calculations for defects and impurities: Applications to III-nitrides, J. Appl. Phys. **95**, 3851 (2004).

[44] T. Gake, Y. Kumagai, and F. Oba, Finite-size corrections for defect-mediated vertical transitions in supercell calculations, arXiv:1907.02380.

[45] C. Gillot and J. Michenaud, Electrical conductivity of similarly doped $BaTiO_3$ single crystals and ceramics in the rhombohedral phase, Solid State Commun. **90**, 23 (1994).

[46] T. Kolodiazhnyi, Insulator-metal transition and anomalous sign reversal of the dominant charge carriers in perovskite $BaTiO_{3-\delta}$, Phys. Rev. B **78**, 045107 (2008).

[47] T. Kolodiazhnyi and S. C. Wimbush, Spin-Singlet Small Bipolarons in Nb-Doped $BaTiO_3$, Phys. Rev. Lett. **96**, 246404 (2006).

[48] Small polarons are also expected to collapse to the delocalized states if an excessive number of small polarons are introduced and/or the temperature is increased; such an insulator-to-metal transition has been commonly reported for heavily doped BTO irrelevant to their dopant species [46,57,58].

[49] T. Kolodiazhnyi, A. Petric, M. Niewczas, C. Bridges, A. Safa-Sefat, and J. E. Greedan, Thermoelectric power, Hall effect, and mobility of n-type $BaTiO_3$, Phys. Rev. B **68**, 085205 (2003).

[50] T. Ohsawa, S. Hirose, and N. Ohashi, Potential barrier formed at domain boundaries in twinned tetragonal $BaTiO_3$ single crystals, Appl. Phys. Lett. **110**, 011604 (2017).

[51] Thermally activated small polaron conductivity seems to be a better fit in cases of polycrystals and/or thin films compared with single crystals [15,17,18,47,57].

[52] A. Janotti, J. B. Varley, M. Choi, and C. G. Van de Walle, Vacancies and small polarons in $SrTiO_3$, Phys. Rev. B **90**, 085202 (2014).

[53] P. E. Blöchl, Projector augmented-wave method, Phys. Rev. B **50**, 17953 (1994).

[54] G. Kresse and D. Joubert, From ultrasoft pseudopotentials to the projector augmented-wave method, Phys. Rev. B **59**, 1758 (1999).

[55] G. Kresse and J. Furthmüller, Efficient iterative schemes for ab initio total-energy calculations using a plane-wave basis set, Phys. Rev. B **54**, 11169 (1996).

[56] We also calculated the STE using the 135-atom supercell with $2 \times 2 \times 2$ Monkhorst-Pack *k*-point sampling. In that case, the resultant error of the self-trapped energies was within 0.06 eV for the R model.

[57] L. Liu, H. Guo, H. L, S. Dai, B. Cheng, and Z. Chen, Effects of donor concentration on the electrical properties of Nb-doped $BaTiO_3$ thin films, J. Appl. Phys. **97**, 054102 (2005).

[58] G. Bouilly, T. Yajima, T. Terashima, W. Yoshimune, K. Nakano, C. Tassel, Y. Kususe, K. Fujita, K. Tanaka, T. Yamamoto, Y. Kobayashi, and H. Kageyama, Electrical properties of epitaxial thin films of oxyhydrides $ATiO_{3x}H_x$ (A = Ba and Sr), Chem. Mater. **27**, 6354 (2015).

[59] K. Momma and F. Izumi, VESTA 3 for three-dimensional visualization of crystal, volumetric and morphology data, J. Appl. Crystallogr. **41**, 653 (2008).